

FRB scattering statistics through the CGM are sensitive to morphology and intermittency

DYLAN L. JOW* ¹ AND CALVIN LEUNG* ^{2,3,4}

¹*Kavli Institute for Particle Astrophysics & Cosmology, Stanford University, Stanford, CA 94305, USA*

²*Department of Astronomy, University of California Berkeley, Berkeley, CA, 94720, USA*

³*Department of Physics, University of California Berkeley, Berkeley, CA, 94720, USA*

⁴*Miller Institute of Basic Research, University of California Berkeley, Berkeley, CA, 94720, USA*

Submitted to ApJL

ABSTRACT

The small-scale properties of circumgalactic gas in ordinary galaxies drive its bulk properties. For instance, the mass loading of cold neutral gas in galactic outflows affects their bulk momentum; gas cooling and shattering processes on small scales affect the spatial distribution of gas in the cool ($T \sim 10^4$ K) circumgalactic medium (CGM). However, hydrodynamical simulations have yet to resolve the CGM on such small scales. Spectroscopy (both absorption and emission) remains our primary probe of the small-scale CGM; however, it is challenging to spatially resolve sub-parsec scales. Fast radio bursts (FRBs)—microsecond to millisecond duration radio pulses—are temporally broadened (“scattered”) by transverse fluctuations in the mean electron density along the line of sight. Critically, the interstellar optics of FRB scattering means that radio pulse scattering is sensitive to transverse electron gradients, often generated by the smallest transverse spatial scales. This makes them a powerful, complementary, and scalable probe of the small-scale CGM on sub-parsec transverse scales. We show that the distribution of scattering timescales introduced by density fluctuations within a single, foreground halo—the tau distribution function, or TDF—is sensitive to the small-scale spatial morphology of the gas. The TDF is readily measurable and is analogous to the areal covering factors reported in quasar absorption statistics. We compute the TDF in two regimes: scattering from a turbulent, volume-filling medium (“volumetric scattering”) distributed along the line of sight; and scattering from discrete structures localized along the line of sight which are both anisotropic and elongated with small volume filling fractions (“intermittent scattering”). Within these regimes, the TDF is sensitive to whether the cool gas comprises primarily spherical, filamentary (1D), or sheet-like (2D) structures. This work sets the stage for upcoming observations which will use hundreds of sight-lines through nearby halos to constrain the ionized, small-scale CGM, and points out a novel science case for FRB detectors like MeerKAT, Parkes, FAST, and the DSA-2000, which are exquisitely sensitive over a narrow field of view.

Keywords: Radio transient sources (2008), Circumgalactic medium, Absorption spectroscopy

1. INTRODUCTION

The multi-phase nature of the circumgalactic medium (CGM) and ubiquitous presence of cool gas ($T \sim 10^4$ K)

has been well established by observation (Rigby et al. 2002; Hennawi et al. 2006; Bowen & Chelouche 2011; Tumlinson et al. 2017). It is thought that this cool phase plays a critical role in determining the central galaxy’s star formation history. However, the presence of cool gas in both star-forming and quiescent galaxies out to large radii has challenged standard pictures of the physics of cold accretion and the evolution of gas in the CGM (Faucher-Giguère & Oh 2023). Questions of the formation and survival of this gas remain unanswered.

dylanjow@stanford.edu

calvin_leung@berkeley.edu

*Equal contribution

Simple analytic descriptions have been proposed, such as the shattering model of [McCourt et al. \(2018\)](#) in which large clouds of warm gas shatter into tiny cloudlets of denser, cool gas with characteristic sizes of $\sim 0.1 - 10$ pc. This model was proposed to explain the high covering factor of cool gas observed in high redshift quasar absorption spectra, as well as explain how cool gas can become entrained in the surrounding hot medium. However, because of the small physical scale potentially associated with this gas, large simulations of the CGM have struggled to reproduce the observed amount and distribution of the cool gas ([Faucher-Giguère & Oh 2023](#)). Moreover, spatial mapping of the velocity fluctuations in CGM emission suggests the presence of a turbulent gas with a Kolmogorov power spectrum ([Chen et al. 2024a,b](#)). While the inner scale of this turbulent cascade is unknown, structure could in principle extend to spatial scales far smaller than accessible to current spectroscopic observations. Uncovering the physical processes that produce and sustain cool gas in the CGM will require new observables that can probe the abundance and morphology of the gas at tiny scales.

Scattering of radio light from fast radio bursts (FRBs) is one such observable. While the amount and nature of scattering expected from the CGM has been debated (see e.g. [Vedantham & Ravi 2019](#); [Ocker et al. 2022](#); [Jow et al. 2024b](#); [Mas-Ribas et al. 2025](#); [Ocker et al. 2025](#)), these authors agree that scattering will be sensitive to electron density fluctuations in cool gas down to tiny (well below parsec) scales.

In this work, we introduce a new observable that is sensitive to the spatial distribution and morphology of cool gas clumps in the CGM. The “scattering timescale distribution function”, or TDF, is the distribution of scattering timescales for an ensemble of FRBs at a fixed effective lensing distance, d_{eff} , intercepting a foreground halo within some specified impact parameter b . Since some scattering-timescale measurements are upper limits, the observed TDF is expressed unambiguously only as a cumulative distribution $f(> \tau_{\text{sc}})$. In this form, $f(> \tau_{\text{sc}})$ can be interpreted as the fraction of sight-lines through a halo with scattering timescales exceeding τ_{sc} . For volumetric scattering by a turbulent medium, the scattering timescale for a given line of sight grows linearly with the effective path length intersecting the cool gas along that sight line. For a cloud complex of cool gas with size, R , and a cool gas volume filling factor, f_V , the mean intersection length through the cool gas is simply $f_V R$. However, the full distribution of intersection lengths is dependent on whether the gas comprises many small spherical cloudlets, filamentary structures, or sheet-like structures. The TDF is determined by the

cumulative distribution of intersection lengths through the gas, and is, therefore, sensitive to the morphology of cool gas on small scales.

Volumetric scattering is characterized by the accumulation of small deflection angles as a ray traverses a volume filling medium. Much of the FRB scattering literature presumes that FRB scattering in the circumgalactic medium will be volumetric ([Ocker et al. 2022](#); [Shin et al. 2025](#); [Ocker et al. 2025](#)). However, refractive scattering due to spatially and/or temporally intermittent structures may also arise ([Jow et al. 2024b](#); [Mas-Ribas et al. 2025](#)). Observations of pulsar scintillation have shown that intermittent scattering, not volumetric scattering, can dominate pulsar scattering angles for at least a few sight-lines in the Milky Way ISM ([Brisken et al. 2010](#); [Zhu et al. 2023](#); [Chen et al. 2025](#)). While the origin of FRB scattering has yet to be definitively localized along the line of sight to the CGM, it is plausible that a similar scenario may be relevant in the CGM. Moreover, the framework for volumetric radio scattering in a turbulent medium commonly employed in the FRB literature assumes the electron density fluctuations are fully described by two-point Gaussian statistics (i.e. a power spectrum) between the inner- and outer-scale of the turbulence. This has, however, been challenged by modern understandings of turbulence, where intermittent structures and higher-order statistics play an important role ([Hopkins 2013](#); [Squire & Hopkins 2017](#); [Beattie et al. 2022](#)). Therefore, we are motivated to make predictions for the TDF of intermittent refractive scattering in addition to volumetric scattering. As we will argue, the TDF of intermittent refractive scattering will likely be dominated by highly elongated structures with large aspect ratios so that the statistics of the scattering timescale will depend on the random inclination angles of these structures relative to the line of sight, which we assume are random.

[Fig. 1](#) summarizes the results of this paper by comparing predictions for the TDF under four different scenarios. In the sections that follow, we will describe how we obtain each of these curves in detail; however, for the moment, we will highlight some salient features of the results. First, we will note that the TDF for volumetric scattering in spherical cloudlets (the blue curve) follows a Gaussian distribution (i.e. an error-function CDF). Volumetric scattering in filamentary and sheet-like cloudlets (orange and green curves) deviates from Gaussian: rays experience a bimodal distribution of path lengths through moderately-inclined and edge-on cloudlets, and, thus, the TDF exhibits a bimodality. The cumulative TDF for volumetric scattering in the aforementioned cases has an exponential drop-off

toward large τ , as the total path length through the scattering medium does not deviate far from the mean (see Section 2). In contrast, the scattering time arising from refractive scattering due to intermittent and highly anisotropic structures with large aspect ratios increases smoothly with the inclination angle of the structure (up to some maximum value). Uniformly random inclination angles yield a TDF with a much shallower power-law drop off (see Section 3).

The true morphology of the cool CGM phase is likely to be highly complex. Thus, we may expect the observed FRB scattering statistics to arise from a combination of the different effects described herein. This work should be regarded as illustrative of the essential fact that the scattering statistics will be sensitive to the scattering regime and morphology, which may provide new insights into the physics of the CGM. While CGM scattering has not been conclusively detected, low-frequency experiments such as CHIME, CHORD, and BURSTT will be exquisitely sensitive to FRB scattering since the signal strength grows as the fourth power of the wavelength λ . For nearby halos which have large extents on the sky, we will have thousands of FRB sight-lines to constrain TDFs towards halos of different masses, assembly histories, and galaxy properties.

2. VOLUMETRIC SCATTERING IN TURBULENT COOL GAS

In this section, we will compute the TDF for complexes of cool gas comprising turbulent cloudlets of different geometries. As we show in Appendix A, a source that is volumetrically scattered by a turbulent medium with a power law spectrum of density fluctuations with sufficiently small inner scale attains a scattering timescale of

$$\begin{aligned} \tau_{\text{sc}} &= \frac{d_{\text{eff}}}{2c} (1+z_l)^3 L \eta, \\ \eta &= A_\beta \lambda^4 r_e^2 \tilde{F}_l n_{e,c}^2, \end{aligned} \quad (1)$$

where $d_{\text{eff}} = d_{sl} d_{lo} / d_{so}$ is a combination of the distances between the source and scattering medium, the scattering medium and observer, and the source and observer. The redshift, z_l , is the redshift of the scattering medium. The quantity, η , is the mean square bending angle per unit length that rays undergo through the scattering medium. It depends on the wavelength, λ , the electron density of the cool gas, $n_{e,c}$, and the fluctuation parameter, \tilde{F}_l , defined in Appendix A. This parameter, \tilde{F}_l , in turn depends on the inner and outer scale of the fluctuations, as well as the variance of the electron density fluctuations evaluated at the outer scale. The term A_β is a numerical term that depends only on the index of the

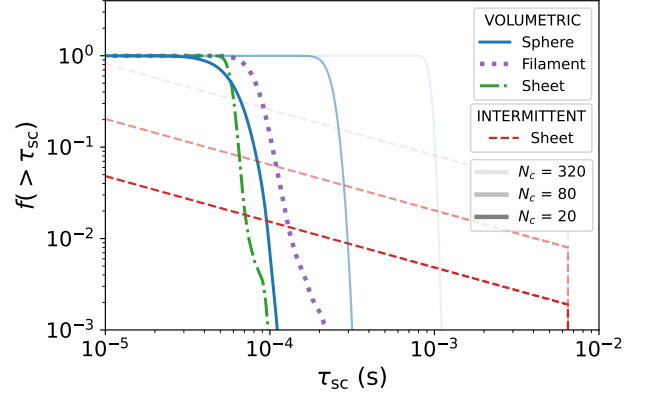


Figure 1. Predictions of the distribution of scattering timescale distribution function (the “TDF”; equivalently the covering factor at a certain scattering timescale) for four different scattering scenarios. (Solid blue) Volumetric scattering due to a complex of size R comprising spherical cool gas cloudlets of uniform radius, r_c , with volume filling factor f_V , such that $f_V R = 0.2 \text{ kpc}$. The different opacity curves are computed for differing cloudlet optical depths, $N_c = 20, 80$ and 320 , which correspond to cloudlets of size $r_c = 10, 2.5$, and 0.625 pc , respectively. We assume a mean-square-bending-angle-per-unit-length of $311 \mu\text{as}^2/\text{pc}$ (see Section 2). We place the scattering surface at a distance of $d_{\text{eff}} = 0.8 \text{ Mpc}$, corresponding to the distance to M31, and set the source wavelength to $\lambda = 75 \text{ cm}$, corresponding to the low-end of the CHIME band. (Dotted purple / dot-dash green) An identical set-up to the blue curve with $N_c = 20$, except the cloudlets are given a filamentary / sheet-like geometry with an aspect ratio of $A = 500$, keeping the volume of the cloudlets fixed in all cases. (Dashed red) Intermittent refractive scattering from corrugated sheets where the sheets have a density of $n_e = 10^{-2} \text{ cm}^{-3}$ and the individual corrugations have an aspect ratio of $A = 10^4$. The distance to the scatterer and wavelength are the same as in the previous cases, as well as $f_V R = 0.2 \text{ kpc}$. The opacity refers to the same values of N_c as before, which correspond to sheet thicknesses of $\delta = 0.16, 0.04$ and 0.01 pc .

power-law spectrum, β . While this expression may seem complicated, the main insight here is that if the properties of the density fluctuations are uniform throughout the cool gas complex, then the TDF of that complex is entirely determined by the distribution of the effective

path length, L , intersecting the cool gas, which we will hereafter refer to as the “intersection length”¹.

Putting some values to these expressions, we obtain

$$\eta = 311 \frac{\mu\text{as}^2}{\text{pc}} \frac{A_\beta}{\Gamma(7/6)} \left(\frac{\lambda}{75 \text{ cm}} \right)^4 \times \left(\frac{\tilde{F}_l}{10^{-3} (\text{pc}^2 \text{ km})^{-1/3}} \right) \left(\frac{n_{e,c}}{10^{-2} \text{ cm}^{-3}} \right)^2. \quad (2)$$

The values for the mean electron density and fluctuation parameter for the cool phase of the CGM are highly unconstrained. Here, we adopt $n_{e,c} = 10^{-2} \text{ cm}^{-3}$ and $\tilde{F}_l = 10^{-3} (\text{pc}^2 \text{ km})^{-1/3}$ as our fiducial values. For Kolmogorov turbulence, $\beta = 11/3$ and the numerical constant is $A_{11/3} = \Gamma(7/6)$. The corresponding scattering timescale is

$$\tau_{\text{sc}} = 0.12 \mu\text{s} (1 + z_l)^{-3} \left(\frac{d_{\text{eff}}}{\text{Mpc}} \right) \left(\frac{L}{\text{pc}} \right) \left(\frac{\eta}{100 \mu\text{as}^2 \text{ pc}^{-1}} \right). \quad (3)$$

In what follows, we will adopt $d_{\text{eff}} = 0.8 \text{ Mpc}$, which corresponds to a source at infinity and a scattering surface at the distance to M31. We choose to focus on nearby halos as they have large extents on the sky and will have many FRB sight-lines through them, enabling constraints on their TDFs. Scattering through the M31 halo, specifically, will be the subject of forthcoming work.

2.1. A single-scale mist

Let us first consider a complex of cool gas of diameter R that comprises many smaller cool cloudlets with uniform radius, r_c . We will assume that these individual cloudlets have uniform electron densities, n_e , and fluctuation parameter, \tilde{F}_l , so that each cloudlet bends rays by the same angle squared per unit distance, η . Thus, the statistics of the scattering time for sight-lines through this complex of cool gas is given by the statistics of the intersection length, L , through the individual cloudlets. Now, let the cool cloudlets have a volume filling fraction f_V of the total volume of the complex. The total number of cloudlets in the complex is $f_V R^3 / r_c^3$, and the average

path length through the cloudlets intersected by a line of sight is $\bar{L} = f_V R$. The average *number* of cloudlets intersected by a sight line (the cloudlet optical depth) is given by

$$N_c = f_V R / r_c. \quad (4)$$

Fig. 2 shows the distribution of L for sight lines through a region of length $R = 1 \text{ kpc}$ filled with spherical cloudlets of radius $r_c = 10 \text{ pc}$, for different volume filling factors, f_V . We compute these distributions numerically by populating a box of dimensions $R \times 20r_c \times 20r_c$ with a number, $f_V R^3 / r_c^3$, of cloudlets with uniform random co-ordinates. A line of sight with a transverse displacement of b relative to the centre of a cloudlet has an intersection length through the cloudlet given by

$$L_c = \begin{cases} 2\sqrt{r_c^2 - b^2} & \text{if } b \leq r_c, \\ 0 & \text{if } b > r_c. \end{cases} \quad (5)$$

For a fine grid of sight-lines through the cloudlet complex, we sum the intersection lengths through every cloudlet that is intersected by the sight line. The resulting distribution is approximately Gaussian with $L/r_c \sim \mathcal{N}(N_c, N_c)$ for $N_c > 1$. Alternatively, we can define

$$\delta L = \frac{L - \bar{L}}{\bar{L}} = \frac{L}{f_V R} - 1, \quad (6)$$

which is distributed according to $\delta L \sim \mathcal{N}(0, N_c^{-1})$.

We want to compute the TDF as a function of τ_{sc} . The result, for $\delta L \sim \mathcal{N}(0, N_c^{-1})$, is

$$f(> \tau) = \frac{1}{2} \text{erfc} \left(\frac{\frac{\tau}{\bar{\tau}} - 1}{\sqrt{2/N_c}} \right), \quad (7)$$

$$\bar{\tau} = \tau_{\text{sc}} \Big|_{L=f_V R}.$$

Here, $\bar{\tau}$ is the mean scattering time due to an intersection length of gas $\bar{L} = f_V R$. Note that distribution of intersection lengths only depends on the complex size, R , and the volume filling factor, f_V , through the combination $f_V R$. The bottom panel of Fig. 2 compares the empirical curves (solid) and the approximate curve (dashed) computed using Eq. 7. The agreement improves for larger N_c , but in either case the qualitative picture is clear: turbulent scattering due to mists produces a sharp cutoff in the $f_{\text{sc}}(> \tau)$ curve above $\tau = \bar{\tau}$.

2.2. Multi-scale mist

In the previous section, we computed the statistics of the intersection length L for a complex of spherical cloudlets with uniform radius. Here we consider a spectrum of cloudlet sizes. The resulting distributions are

¹ It is common in the scattering literature (e.g. Cordes et al. 2022, 2016; Ocker et al. 2022; Shin et al. 2025), to replace the factor of $d_{\text{eff}} L n_{e,c}^2 / 2$ in Eq. 1 with $\text{DM}_l^2 G_{\text{scatt}}$, where $\text{DM}_l = L n_{e,c}$ is the excess dispersion measure from the scattering material and $G_{\text{scatt}} = d_{\text{eff}} / 2L$ is called the “geometric leverage” factor. The advantage of writing Eq. 1 in this way is to relate the predicted scattering with a potentially observable quantity, DM_l . However, for our purposes, this formulation obscures the simple linear relationship between scattering timescale and intersection length.

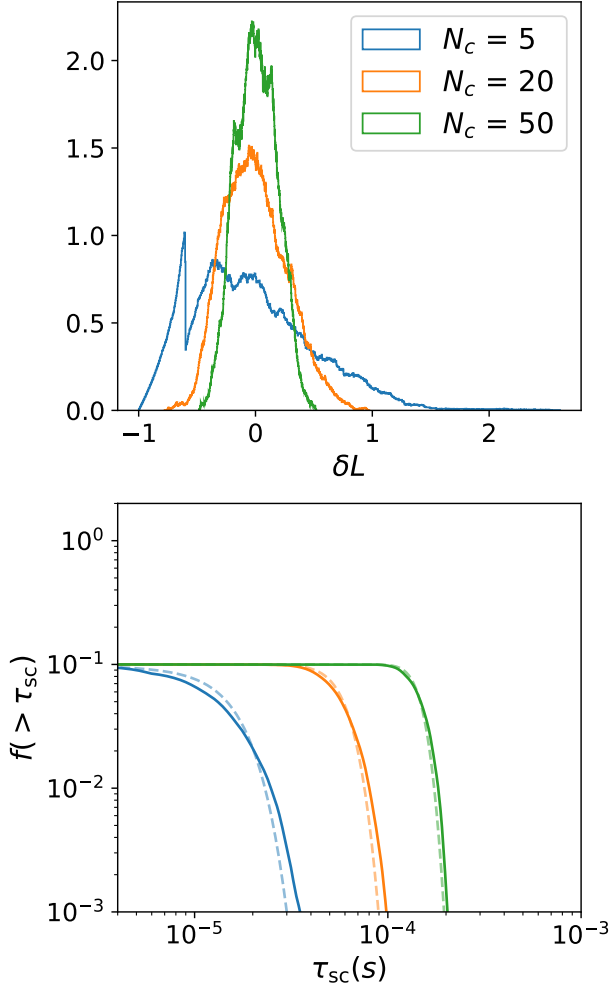


Figure 2. (Top) Distribution of intersection lengths for a complex of spherical cloudlets with radius $r_c = 10$ pc and different cloudlets optical depths, $N_c = f_V R / r_c$. The distributions become narrower as N_c increases. (Bottom) The solid lines show the cumulative distribution functions for the scattering timescale (assuming $\eta = 311 \mu\text{as}^2/\text{pc}$ and $d_{\text{eff}} = 0.8$ Mpc) for the above intersection length distributions. The upper x -axis on the right panel shows the intersection length converted to a scattering time for $d_{\text{eff}} = 0.8$ Mpc and $\eta = 311 \mu\text{as}^2/\text{pc}$. The dashed lines show the analytic approximation derived assuming that the above distributions follow $\delta L \sim \mathcal{N}(0, N_c^{-1})$.

the same, with the exception that the cloudlet optical depth must be modified.

Consider spherical cloudlets with a power-law distribution of radii,

$$P(r_c) \propto r_c^{-a}, \quad (8)$$

between some minimum and maximum sizes, $r_{c,\text{min}}$ and $r_{c,\text{max}}$. Let f_V be the volume filling factor of the cloudlets in a region of volume V . The total number

of cloudlets in that region is

$$\begin{aligned} n_V &= f_V V / \int_{r_{c,\text{min}}}^{r_{c,\text{max}}} P(r_c) \frac{4}{3} \pi r_c^3 dr_c, \\ &= f_V V \frac{3}{4\pi} \frac{4-a}{1-a} \frac{z_{c,\text{max}}^{1-a} - z_{c,\text{min}}^{1-a}}{z_{c,\text{max}}^{4-a} - z_{c,\text{min}}^{4-a}}. \end{aligned} \quad (9)$$

The average intersection length for lines of sight through the gas complex is given by

$$\bar{L} = \int_{r_{c,\text{min}}}^{r_{c,\text{max}}} r_c \frac{\pi r_c^2}{A} n_V P(r_c) dr_c, \quad (10)$$

where A is the corresponding sky area of the total volume. Evaluating the integral, one obtains $\bar{L} = f_V R$, as expected.

Now, we will define an effective cloudlet optical depth to be the minimum number of intersected clouds:

$$N_c = f_V R / r_{c,\text{max}}. \quad (11)$$

So long as $N_c > 1$, the largest cloudlets dominate the variance of the intersection length distribution, and one finds that $\delta L \sim \mathcal{N}(0, N_c^{-1})$, as with the single-scale mist. It follows that the form of the TDF is identical to Eq. 7, except that the effective optical depth, N_c , is modified to be referenced to the largest cloud size (see Fig. 3).

2.3. Sheets and filaments versus cloudlets

In arguing that the statistics of the scattering timescale are highly dependent on the statistics of the intersection length through the cool gas, it becomes clear that the scattering timescale statistics are sensitive to the geometry of the cool gas. Here we will compare three simple scenarios as illustrative of this point: gas comprising cloudlets in the shapes of spheres, filaments, and sheets. The intersection length through a filament or sheet is highly dependent on the inclination angle of the object relative to the line of sight, unlike a sphere. Thus, the statistics of the intersection lengths through filaments and sheets will deviate from the simple Gaussian distribution that we have already shown characterizes spherical cloudlets.

For a sphere of radius r_c , Eq. 5 gives the intersection length through the sphere at an impact parameter of b from the centre. Consider now a rectangular filament of dimension $\delta \times \delta \times \Lambda$, with $\delta \ll \Lambda$. Let $\hat{n} = (\sin \theta \cos \phi, \sin \theta \sin \phi, \cos \theta)$ be the vector pointing along the long edge of the filament, and let θ be the inclination angle relative to the line of sight (see Fig. 4 for a diagram showing the geometric parameters). We take the intersection length through a filament centred

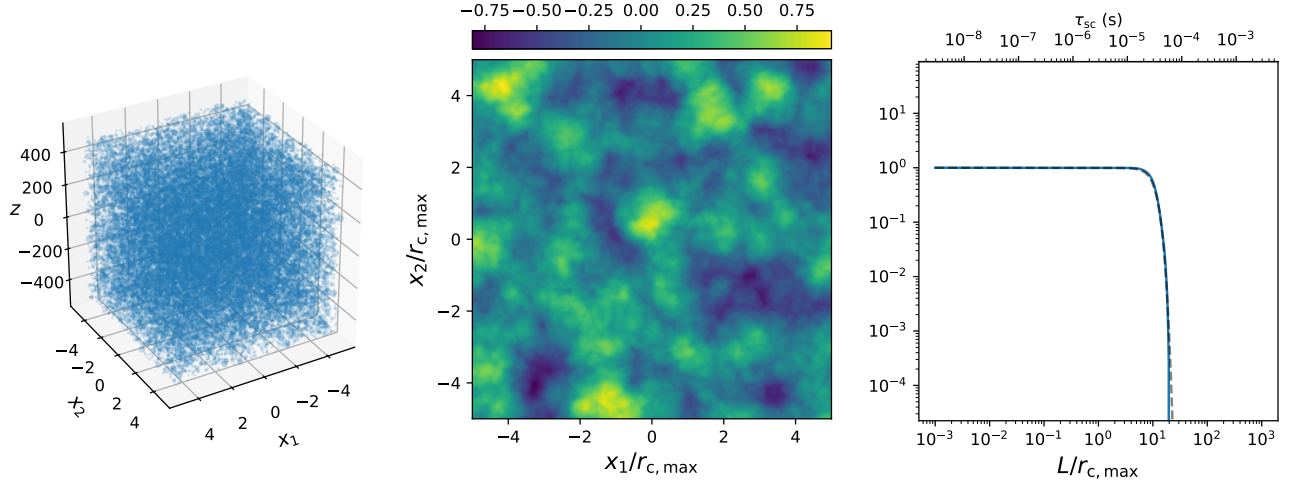


Figure 3. A simulation of intersection lengths through a complex of spherical cloudlets with a power-law distribution of radii ($\alpha = 2$, $r_{c,\min} = 0.1$ pc, $r_{c,\max} = 10$ pc). The left panel shows the mist of cloudlets, randomly distributed in a box of dimensions $10r_{c,\max} \times 10r_{c,\max} \times R$, with $R = 1$ kpc. The co-ordinate axes are in units of $r_{c,\max}$. The middle panel shows the intersection length contrast, $\delta L = (L - \bar{L})/\bar{L}$, for a grid of vertical sight-lines through the box, and the right shows the cumulative distribution function of these intersection lengths in blue. The dashed line shows the analytic curve for a Gaussian distribution (Eq. 7).

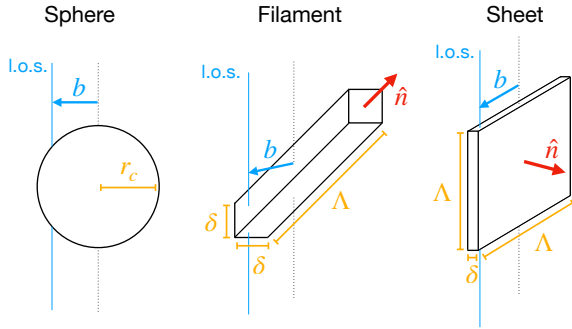


Figure 4. Diagram showing the geometric parameters used in Eqs. 5, 12, and 13 to define the intersection length through a spherical, filamentary, or sheet-like cloudlet, for a line of sight with impact parameter \mathbf{b} from the centre of the cloudlet.

at the origin, intersected by the line of sight to be

$$L_c^{\text{filament}}(\mathbf{b}) = \begin{cases} \min \left\{ \frac{\delta}{|\sin \theta|}, \Lambda \right\}, & \tilde{b}_y < \delta \text{ and} \\ & \tilde{b}_x < \max \left\{ \frac{\Lambda}{2} |\sin \theta|, \frac{\delta}{2} \right\} \\ 0 & \text{else,} \end{cases} \quad (12)$$

where $\tilde{b}_x = b_x \cos \phi + b_y \sin \phi$ and $\tilde{b}_y = -b_x \sin \phi + b_y \cos \phi$. The conditions on \tilde{b}_x, \tilde{b}_y ensure that the line of sight passes through the filament. When the inclination angle is shallow, the intersection length is just the thickness $\delta/|\sin \theta|$. However, when the inclination angle is sufficiently large, the line of sight passes through the

entire length of the filament, Λ . Since Λ sets an upper bound, we take the minimum of these two values for simplicity.

Now consider a sheet of dimension $\delta \times \Lambda \times \Lambda$ with $\delta \ll \Lambda$. Let \hat{n} be the vector normal to the face of the sheet (see Fig. 4). The intersection length for a sheet centred at the origin is

$$L_c^{\text{sheet}}(\mathbf{b}) = \begin{cases} \min \left\{ \frac{\delta}{|\hat{n} \cdot \hat{z}|}, \Lambda \right\}, & \tilde{b}_y < \delta \text{ and} \\ & \tilde{b}_x < \max \left\{ \frac{\Lambda}{2} |\hat{n} \cdot \hat{z}|, \frac{\delta}{2} \right\} \\ 0 & \text{else.} \end{cases} \quad (13)$$

Fig. 5 shows a comparison of the distributions of intersection lengths for a cool gas complex with $Rf_V = 0.2$ kpc. For the spherical clouds, we choose a radius of $r_c = 10$ pc. We fix the volume to be the same for the filaments and sheets, such that for the filaments $\frac{4}{3}\pi r_c^3 = \delta^2 \Lambda$ and for the sheets $\frac{4}{3}\pi r_c^3 = \delta \Lambda^2$. Thus, the gas complex has the same number of objects in each case, which we randomly distribute throughout the total volume. This leaves the choice of the aspect ratio, which we take for both the filaments and sheets to be $\Lambda/\delta = 500$. The top row shows the intersection length projected onto the sky. The qualitative difference between spheres, filaments, and sheets is readily apparent. The largest values for the filament case are dominated by roughly square regions where the filament is parallel to the line of sight. The largest values for the sheet case are dominated by thin streaks representing the edge of

the sheet when the sheet is parallel to the line of sight. The bottom row shows the distribution of the deviations of the intersection lengths from the mean, δL . In all cases, the mean intersection length is roughly given by $\bar{L} = f_V R$ as expected. The left panel of Fig. 6 compares the resulting TDF. All three distributions share the same mean, $\bar{\tau}$, corresponding to the mean intersection length; however, the extended tails of the filament and sheet distributions cause the TDF to deviate from the simple Gaussian expectation.

3. INTERMITTENT REFRACTIVE SCATTERING

In the previous section, we considered volumetric scattering through a statistically isotropic medium characterized by a power spectrum of density fluctuations. In that setting, scattering is determined by the mean-square bending angle per unit path length. The scattering statistics are then determined by the total length a given line of sight intersects the scattering medium. Different morphologies of the gas may give rise to distinguishable statistics in the observed scattering timescales. However, this framework relies on a few key assumptions. Firstly, it assumes that the scattering is volumetric; i.e., rays accrue small deflections continuously as they propagate through the medium. Secondly, it assumes that the medium responsible for scattering is statistically isotropic and characterized by a power spectrum of density fluctuations. This is in contrast with *intermittent* scattering, where the scattering angle is dominated by a small number of coherent structures along the line of sight.

Both of these assumptions have been challenged in different contexts. Studies of turbulence have begun to emphasize the importance of spontaneous formation of intermittent structures in turbulent media (Hopkins 2013; Squire & Hopkins 2017; Beattie et al. 2022). Modeling a turbulent medium as a Gaussian random field with a power-law power spectrum is likely to miss important effects even for standard Kolmogorov turbulence. Moreover, detailed study of a few nearby pulsars has shown that scattering through at least some lines of sight through the ISM is dominated by intermittent structures (Brisken et al. 2010; Zhu et al. 2023; Chen et al. 2025). Similarly, cosmic ray observations have begun to paint a similar picture: intermittent, coherent structures in the ISM may be predominantly responsible for the scattering of low-energy (MeV - TeV) cosmic rays (Butsky et al. 2024). Thus, both theoretical considerations and observational results across multiple domains point to the increasing relevance of intermittency to models of the ISM. The CGM, of course, is a very different context from the ISM. However, in the absence of observations

indicating one way or another, when making predictions for radio scattering in the CGM, we should not dismiss the possibility that intermittent structures may play an important role. Thus, in this section, we consider possible sources of intermittent scattering in the CGM.

3.1. Refractive scattering from smooth, spherical clouds

As Jow et al. (2024b) argue, even if the inner scale of the turbulence is too large to produce significant volumetric scattering, cool gas cloudlets can still produce significant large-scale refractive scattering if the electron densities are sufficiently high. In that scenario, each cloudlet acts as a single, smooth plasma lens. If the bending angle is sufficiently large, an ensemble of such cloudlets can produce many images that will be observed as a scattering tail.

A light ray propagating through a plasma accrues a bending angle of

$$\alpha = (1 + z_l)^{-2} \frac{\lambda^2 r_e}{2\pi} \nabla_{\perp} N_e, \quad (14)$$

where $\nabla_{\perp} N_e$ refers to the gradient of the electron column density perpendicular to the line of sight. The wavelength, λ , is the observing wavelength, and so the bending angle has a factor of $(1 + z_l)^{-2}$, where z_l is the redshift of the scattering surface. For a spherical cloudlet of electrons, the column density is related to the 3D density by $N_e = r_c n_e$, where r_c is the size of the cloudlet. For a smoother, spherical cloudlet, the column density gradient can be estimated by $\nabla_{\perp} N_e \sim N_e / r_c \sim n_e$. Thus, the bending power of a spherical cloudlet is roughly

$$\alpha_{\text{sphere}} \sim (1 + z_l)^{-2} \frac{\lambda^2 r_e n_e}{2\pi}. \quad (15)$$

In order to form multiple images, more than one ray needs to be bent into the observer's line of sight. The maximum transverse distance to the unperturbed line of sight that a lens can be placed while still bending rays that intersect the observer is $x = \alpha d_{\text{eff}}$. The criterion for a lens to form multiple images is that this distance be greater than the transverse size of the lens itself: $x > r_c$. The ratio x/r_c is precisely the convergence of the lens, κ (see Jow et al. 2024b), and is given by

$$\begin{aligned} \kappa_{\text{sphere}} \sim 0.03 (1 + z_l)^{-2} & \left(\frac{\lambda}{75 \text{ cm}} \right)^2 \left(\frac{d_{\text{eff}}}{1 \text{ Gpc}} \right) \\ & \times \left(\frac{n_e}{10^{-2} \text{ cm}^{-3}} \right) \left(\frac{r_c}{10 \text{ pc}} \right)^{-1}. \end{aligned} \quad (16)$$

Thus, for typically presumed parameters for cool gas in the CGM, a single spherical cloud does not have

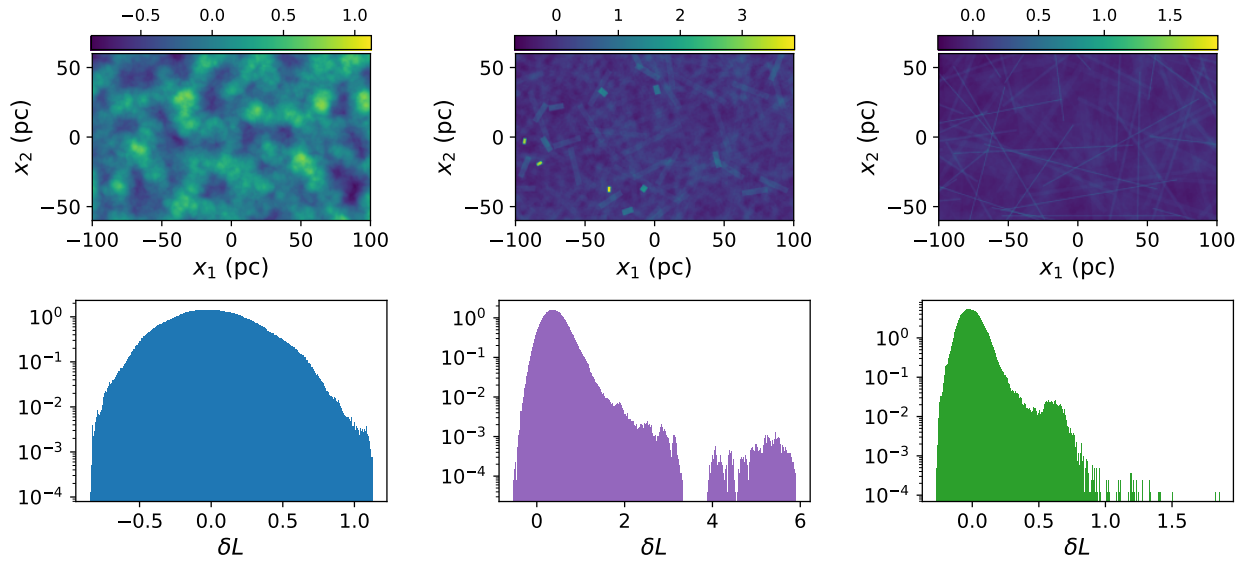


Figure 5. (Top row) The intersection lengths of a mist of spherical (left), filamentary (middle), and sheet-like (right) cloudlets through a box of dimension $0.2 \text{ kpc} \times 0.2 \text{ kpc} \times 1 \text{ kpc}$. The spheres have uniform radius $r_c = 10 \text{ pc}$. The filaments have dimension $\delta \times \delta \times \Lambda$ and the sheets have dimension $\delta \times \Lambda \times \Lambda$, where in both cases we choose $\Lambda/\delta = 500$. The smaller dimension is chosen so that the volume of each object is equal to the $\frac{4}{3}\pi r_c^3$. Each box is randomly populated with cloudlets to have a volume filling factor of $f_V = 0.2$. The colour map shows the intersection length contrast $\delta L = (L - \bar{L})/\bar{L}$ where $\bar{L} = f_V R$. (Bottom row) The distribution of the intersection length contrast values in the top row.

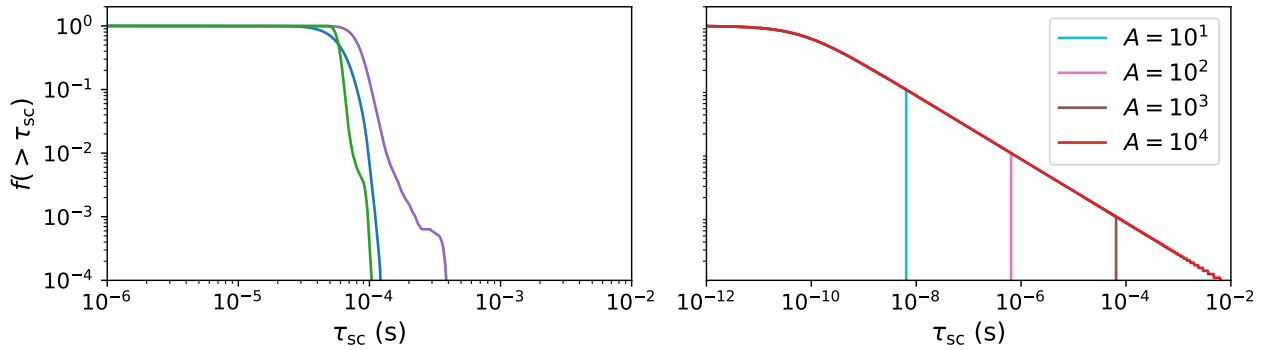


Figure 6. (Left) The cumulative TDF for volumetric scattering through complexes with spherical, filamentary, and sheet-like cool gas clumps (derived from the intersection length distributions shown in Fig. 5). The intersection lengths are converted to scattering times with $\eta = 311 \mu\text{as}^2/\text{pc}$ and $d_{\text{eff}} = 0.8 \text{ Mpc}$. (Right) The cumulative TDF for intermittent scattering from a complex of corrugated sheets with $N_c = 1$ and varying aspect ratios. We assume the sheets have uniform density $n_e = 10^{-2} \text{ cm}^{-3}$ and are at a distance of $d = 0.8 \text{ Mpc}$. The y -axis is the same as the left plot.

sufficient bending power to produce multiple refractive images ($\kappa < 1$). An ensemble of such cloudlets has a collective convergence of $\kappa_{\text{tot}} \sim \sqrt{N_c} \kappa_{\text{sphere}}$, where $N_c = f_V R/r_c$ is the average number of cloudlets that intersect a given line of sight. In order for an ensemble of such cloudlets to produce many refractive images, hundreds of cloudlets would need to be intersected by the average line of sight. Therefore, if the cool gas comprises spherical cloudlets with $\sim 10 \text{ pc}$ characteristic scales, we do not expect significant refractive scattering, consis-

tent with Mas-Ribas et al. (2025). Note, however, that the total number of refractive images that are formed is roughly $\sim \kappa_{\text{tot}}^2$. This scales only linearly with the volume filling factor, but is highly sensitive to the cloud size at fixed f_V , scaling as $\sim r_c^{-3}$. Thus, even if only a small fraction of the total volume of cloudlets comprises sub-parsec cloudlets, intermittent refractive scattering is still possible from spherical cloudlets without invoking a power spectrum of internal density fluctuations.

3.2. Corrugated sheets

In this section, we consider intermittent, refractive scattering from corrugated sheet structures. High aspect-ratio sheet structures have been proposed for the morphology of the warm neutral interstellar medium (Heiles & Troland 2003); in recent decades, observations of pulsar scintillation have further revealed that radio scattering in the warm ionized medium is often dominated by a small number of intermittent and isotropic, refractive scatterers. Elongated sheet structures that are inclined along the line of sight have been invoked to alleviate the so-called “over-pressure problem” which arises from the assumption that the scattering structures are spherical. Briefly, \sim mas bending angles that are routinely observed in pulsar scintillation, if generated by spherical small-scale scattering structures, yield measurements of the electron density (Eq. 15) that are three-orders of magnitude over-pressured relative to the ambient ISM. Anisotropic scatterers – slabs with large ($\sim 10^3$) aspect ratios – alleviate this problem, since the bending angle is enhanced by a factor of the aspect ratio, A (see Appendix B). For a slab of electrons with density n_e , and aspect ratio A , the bending angle as a function of the slab’s inclination ι relative to the line of sight is

$$\alpha(\iota) = (1 + z_l)^{-2} \frac{\lambda^2 r_e n_e}{2\pi} \min\{\tan \iota, A\}. \quad (17)$$

Heiles & Troland (2003) propose a “blobby sheet” morphology for the neutral phase of the ISM; Pen & Levin (2014); Simard & Pen (2018); Jow et al. (2024a) propose corrugated sheets in the warm ionized ISM to explain both pulsar scintillation and extreme scattering event phenomenology. This motivates our consideration of similar corrugated-sheet structures in the CGM, which can be divided into two regimes (see Fig. 7). These two regimes are distinguished by the radius of curvature of the corrugations, with “accordions” featuring a small radius of curvature and lasagnas featuring a large radius of curvature. We can approximate each individual corrugation as a slab of length Λ and thickness δ (shown in blue). Pen & Levin (2014) argue that current sheets in the ISM can explain pulsar scintillation observations. These current sheets are sustained by anti-parallel magnetic fields on either side of the sheet. Small transverse perturbations propagate along the sheet as shallow waves, forming lasagna-like corrugations.

In the CGM, magnetic fields may act to form accordion-like corrugated sheets. McCourt et al. (2018) originally proposed that slightly overdense gas in the CGM shatters into tiny spherical cloudlets as it cools, with a characteristic radius set by the sound speed times the cooling time. Later, hydrodynamical simulations confirmed this picture. However, magnetic fields likely

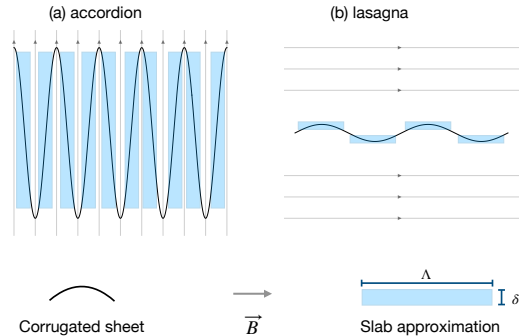


Figure 7. Diagram of the two kinds of corrugated sheets: “accordion”, with tight curvature radii, and “lasagna”, with large curvature radii. Anisotropic gas with large aspect ratios can naturally form in magnetized regions, with a general expectation that accordion-like sheets will form with the corrugations parallel to the magnetic field, and lasagna-like sheets will form with the corrugations transverse to the magnetic field. In this work, for simplicity, we treat corrugated sheets as organized collections of individual corrugations or slabs (shown in blue), with fixed length Λ and width δ .

play an important role in the gas dynamics of the CGM, and will likely induce anisotropy in the cool gas structures. Wang et al. (2025) find that magnetic pressure prevents shattering into spherical clouds. Instead, gas is confined to flow parallel to the magnetic fields, and counter-streaming motions produce accordion-like sheets. While the physics of the CGM is uncertain, highly anisotropic sheets (with large aspect ratios) have been seen to be produced in the presence of magnetic fields across multiple contexts. Thus, we are motivated to study their scattering properties. Accordion-like sheets occur when corrugations form parallel to the magnetic field, whereas lasagna-like sheets occur when corrugations form transverse to the magnetic field. In either case, the scattering phenomenology is essentially identical. The most salient feature of corrugated sheets is the presence of many, organized slabs of similar density and aspect ratio.

Since the bending angle is enhanced by a factor of the aspect ratio, the lens convergence for an edge-on corrugated sheet is

$$\kappa_{\text{sheet}} \sim A \times 0.03 (1 + z_l)^{-2} \left(\frac{\lambda}{75 \text{ cm}} \right)^2 \left(\frac{d_{\text{eff}}}{1 \text{ Gpc}} \right) \times \left(\frac{n_e}{10^{-2} \text{ cm}^{-3}} \right) \left(\frac{\delta}{10 \text{ pc}} \right)^{-1}. \quad (18)$$

Thus, a relatively modest aspect ratio of 100 : 1 can produce many refractive images, when the sheet is edge-on.

Now, we want to compute the statistics of the scattering time. The scattering time as a function of inclination angle for a single sheet is $\tau_{\text{corr}}(\iota) = d_{\text{eff}}\alpha_{\text{sheet}}(\iota)^2/2c$, where we take the characteristic bending angle $\alpha_{\text{sheet}}(\iota)$ to be half the maximum bending angle (see Appendix B). The scattering time is a monotonically increasing function of inclination angle with $\iota \in [0, \pi/2]$ (i.e. the scattering time increases as the sheet becomes more inclined). Thus, for a single corrugated sheet, the probability that the sheet produces a scattering time τ_{sc} is simply $P(\iota > \iota^*)$, where ι^* is defined such that $\tau_{\text{corr}}(\iota^*) = \tau_{\text{sc}}$. Assuming a uniform random distribution of inclination angles over a sphere, this probability is just $\cos(\iota^*)$ or, approximately $\pi/2 - \iota^*$ for nearly edge-on inclinations.

Now, consider a complex of gas of size R filled with thin, corrugated sheets with uniform thickness δ . In Appendix B, we find that the average number of sheets intersected by the line of sight through such a complex is given by

$$N_c = \frac{1}{2\pi(1 + \log A)} \frac{f_V R}{\delta}. \quad (19)$$

Then, in the limit of low optical depth ($N_c < 1$), the probability of exceeding a scattering timescale of τ_{sc} is given by

$$f(> \tau_{\text{sc}}) = N_c \cos \iota^*. \quad (20)$$

This can be regarded as the optical depth of scattering with $\tau > \tau_{\text{sc}}$, so that for large N_c , one obtains a TDF of

$$f(> \tau_{\text{sc}}) = 1 - \exp\{-N_c \cos \iota^*\}. \quad (21)$$

The right panel of Fig. 6 shows $f(> \tau_{\text{sc}})$ for a complex of cool gas filled with corrugated sheets of varying aspect ratio such that $N_c = 1$. For a complex of size $R = 1$ kpc, a sheet thickness of $\delta = 1$ pc, and an aspect ratio of $A = 1000$, this corresponds to a volume filling factor of $f_V = 0.05$. The curves are identical for different aspect ratios up until they hit the maximum scattering time, which is set by

$$\begin{aligned} \tau_{\text{max}} &= \frac{d_{\text{eff}}}{32\pi^2 c} (1 + z_l)^{-3} \lambda^4 r_e^2 n_e^2 A^2, \\ &= 0.08 \text{ s } (1 + z_l)^{-3} \left(\frac{d_{\text{eff}}}{1 \text{ Gpc}} \right) \left(\frac{\lambda}{75 \text{ cm}} \right)^2 \\ &\quad \times \left(\frac{n_e}{10^{-2} \text{ cm}^{-3}} \right)^2 \left(\frac{A}{10^3} \right)^2. \end{aligned} \quad (22)$$

Note that, unlike volumetric scattering, the $f(> \tau_{\text{sc}})$ curve has a shallow drop-off until it reaches τ_{max} . The curves are all the same up until this point, because Eq. 17 is independent of the geometric parameters of the sheet up to $\tan \iota = A$.

Here we have focused on intermittent scattering from corrugated sheets, which we have modelled as an organized collection of slabs with some fixed aspect ratio. We might instead consider the intermittent scattering from a collection of filaments with random orientations. However, the probability that a filament is highly inclined relative to the line of sight is suppressed relative to the probability for a sheet. Namely, if \hat{n} defines the orientation of the filament and lies parallel to the filament (see Fig. 4), then the filament is parallel to the line of sight when $\iota = 0$. The scattering time increases monotonically with *decreasing* ι , and therefore the probability that the scattering timescale exceeds some threshold is given by $P(\iota < \iota^*) \sim \iota^{*2}$. In other words, for equivalent aspect ratios, it is less likely for a filament to be nearly aligned with the line of sight than it is for a sheet, as in the former case \hat{n} must be close to the pole and in the latter case \hat{n} only needs to lie near the equator.

4. DISCUSSION

In this paper, we have examined different possible scenarios for scattering in the CGM. We consider two broad categories: volumetric scattering and intermittent scattering. In the former case, scattering occurs due to the small, random angles that a ray accrues as it propagates through an isotropic, volume-filling medium characterized by a power spectrum of density fluctuations. In the latter case, intermittent structures in the medium dominate the scattering. In both cases, the resulting statistics of the scattering depends strongly on the geometry of the cool gas. In particular, we consider scenarios where all of the gas is either in spherical, filamentary, or sheet-like structures. Spherical cloudlets have been shown to form when over-densities cool faster than their sound crossing time, shattering into a mist of spherical cloudlets (McCourt et al. 2018; Gronke & Oh 2020). In the presence of magnetic fields, these shattered cloudlets can become highly anisotropic with large aspect ratios (Wang et al. 2025). Filamentary structures may naturally form when spherical cloudlets become entrained in the hot gas, forming cometary tails as they move within the hot phase (McCourt et al. 2015). Thus, determining the morphology of the cool gas through FRB scattering may directly implicate the physical processes at work in the CGM at small scales. In reality, it is likely that the cool phase of the ionized CGM exhibits a mixture of morphologies; this work should be regarded as an illustration of the effects that may be present.

The statistics of volumetric scattering are determined by the total path length through the scattering material. In contrast, intermittent scattering is likely to be dominated by highly anisotropic structures with large

aspect ratios, as these are precisely the structures that can produce large column density gradients, without excessive intrinsic densities. Therefore, the statistics of intermittent scattering are determined by the random orientations of the structures relative to the line of sight. Whether scattering in the CGM will be dominated by volumetric scattering or intermittent scattering is unknown. However, it is worth noting that pulsar scintillation observations have revealed the presence of intermittent refractive scattering sites in the ISM for some sight-lines (Zhu et al. 2023; Chen et al. 2025). Similarly, recent observations of cosmic rays have suggested that low-energy cosmic rays are also scattered not volumetrically in the ISM but by a small number of coherent and intermittent structures: potentially the very same structures that are responsible for pulsar scintillation and extreme scattering events (Kempster et al. 2025). Moreover, while the volumetric scattering formalism that has been used here is commonly employed in the FRB scattering literature (e.g. Cordes et al. 2016; Ocker et al. 2021), Eq. 1 is ultimately derived assuming that the underlying turbulent medium is well-characterized by a power spectrum (i.e. its two-point statistics) (see Appendix A). This simple picture of turbulence is inconsistent with modern understandings of turbulence. The so-called “intermittency modeling” paradigm of turbulence studies increasingly emphasizes the importance of spontaneous, coherent and intermittent structure in the morphology and dynamics of turbulent media. Bridging the gap between FRB scattering observations and the physics of the CGM will require moving beyond simple scattering prescriptions.

By introducing the tau distribution function (TDF), this work provides a conceptually simple framework that may be applied to observations to begin to probe the microphysics of the CGM. However, since there are many potential sources of scattering outside of intervening CGM halos (including the Milky Way and host ISM), and since, in practice, scattering often falls below detectability thresholds, there remain practical challenges in directly measuring the TDF for a given halo. By taking the total amount of observed scattering from all contributions as an upper limit on the amount of scattering that can be contributed by a halo, the TDF may observationally be constrained (Leung et al., in prep). A significant limitation to this approach arises from the unknown intrinsic TDF of the FRB host environment. Localization of sources may enable the removal of FRBs in environments which are likely to significantly domi-

nate the observed scattering (such as FRBs in edge-on galaxies or active star forming regions). Alternatively, selecting FRBs without any foreground halos may enable a measurement of the intrinsic TDF, which can then be accounted for when placing constraints on the TDF of intervening halos. Further exploration of these practical issues will be the subject of forthcoming work.

5. CONCLUSION

In this paper, we have proposed to measure the scattering timescale distribution function, or TDF, of intervening galaxy halos to characterize their CGM. We have revisited the volumetric scattering formalism originally parameterized by Cordes et al. (2016), and have shown that the mean-square bending angle per unit length is the fundamental quantity which characterizes “volumetric scattering” sourced by a power spectrum of density fluctuations. The scattering time then scales linearly with the path length through the scattering material, multiplied by this mean-square bending angle. In addition, we have written concrete predictions for “intermittent scattering”, sourced not by a power spectrum of density fluctuations within turbulent gas clumps, but, instead, by the bulk geometry of coherent filamentary or sheet-like structures with large aspect ratios. In both of these scenarios, we have shown that the distribution of FRB scattering timescales—or simply, the TDF—is sensitive to small-scale density fluctuations in the ionized CGM. In a power spectrum formalism, this scale can be as small as the “inner scale” which is difficult to resolve both observationally and even in modern hydrodynamical simulations. This work concretely demonstrates the potential to probe the CGM using deep, narrow-field FRB observations. Sensitive, narrow-field telescopes like MeerKAT, FAST, and Murriyang, with repeated visits to single fields, could excel at providing dense grids of FRBs. For intervening halos at $\lesssim 100$ Mpc, the FRB backlights used need not be localized (as d_{eff} is effectively known *a priori*). Widefield drift-scan telescopes like CHIME or BURSTT will also rapidly build up exposure time towards large solid angles on the sky.

6. ACKNOWLEDGMENTS

We gratefully acknowledge Vicky Kaspi, Daniel Amouyal, Stella Ocker, and the CHIME/FRB Collaboration for helpful comments and discussions.

Software: `numpy` (Harris et al. 2020), `matplotlib` (Hunter 2007)

REFERENCES

- Beattie, J. R., Mocz, P., Federrath, C., & Klessen, R. S. 2022, *MNRAS*, 517, 5003, doi: [10.1093/mnras/stac3005](https://doi.org/10.1093/mnras/stac3005)
- Bowen, D. V., & Chelouche, D. 2011, *APJ*, 727, 47, doi: [10.1088/0004-637X/727/1/47](https://doi.org/10.1088/0004-637X/727/1/47)
- Briskin, W. F., Macquart, J.-P., Gao, J. J., et al. 2010, *APJ*, 708, 232, doi: [10.1088/0004-637X/708/1/232](https://doi.org/10.1088/0004-637X/708/1/232)
- Butsky, I. S., Hopkins, P. F., Kempster, P., et al. 2024, *MNRAS*, 528, 4245, doi: [10.1093/mnras/stae276](https://doi.org/10.1093/mnras/stae276)
- Chen, M. C., Chen, H.-W., Rauch, M., et al. 2024a, arXiv e-prints, arXiv:2410.14785, doi: [10.48550/arXiv.2410.14785](https://doi.org/10.48550/arXiv.2410.14785)
- . 2024b, *ApJ*, 962, 98, doi: [10.3847/1538-4357/ad1406](https://doi.org/10.3847/1538-4357/ad1406)
- Chen, Y.-H., Siegel, S., Baker, D., Pen, U.-L., & Stinebring, D. 2025, *APJ*, 990, 91, doi: [10.3847/1538-4357/ade4c0](https://doi.org/10.3847/1538-4357/ade4c0)
- Cordes, J. M., Ocker, S. K., & Chatterjee, S. 2022, *APJ*, 931, 88, doi: [10.3847/1538-4357/ac6873](https://doi.org/10.3847/1538-4357/ac6873)
- Cordes, J. M., & Rickett, B. J. 1998, *APJ*, 507, 846, doi: [10.1086/306358](https://doi.org/10.1086/306358)
- Cordes, J. M., Wharton, R. S., Spitler, L. G., Chatterjee, S., & Wasserman, I. 2016, arXiv e-prints, arXiv:1605.05890. <https://arxiv.org/abs/1605.05890>
- Faucher-Giguère, C.-A., & Oh, S. P. 2023, *ARAA*, 61, 131, doi: [10.1146/annurev-astro-052920-125203](https://doi.org/10.1146/annurev-astro-052920-125203)
- Gronke, M., & Oh, S. P. 2020, *MNRAS*, 494, L27, doi: [10.1093/mnras/slaa033](https://doi.org/10.1093/mnras/slaa033)
- Harris, C. R., Millman, K. J., van der Walt, S. J., et al. 2020, *Nature*, 585, 357, doi: [10.1038/s41586-020-2649-2](https://doi.org/10.1038/s41586-020-2649-2)
- Heiles, C., & Troland, T. H. 2003, *ApJ*, 586, 1067, doi: [10.1086/367828](https://doi.org/10.1086/367828)
- Hennawi, J. F., Prochaska, J. X., Burles, S., et al. 2006, *APJ*, 651, 61, doi: [10.1086/507069](https://doi.org/10.1086/507069)
- Hopkins, P. F. 2013, *MNRAS*, 430, 1880, doi: [10.1093/mnras/stt010](https://doi.org/10.1093/mnras/stt010)
- Hunter, J. D. 2007, *Computing in Science & Engineering*, 9, 90, doi: [10.1109/MCSE.2007.55](https://doi.org/10.1109/MCSE.2007.55)
- Jow, D. L., Pen, U.-L., & Baker, D. 2024a, *MNRAS*, 528, 6292, doi: [10.1093/mnras/stae300](https://doi.org/10.1093/mnras/stae300)
- Jow, D. L., Wu, X., & Pen, U.-L. 2024b, *Proceedings of the National Academy of Science*, 121, e2406783121, doi: [10.1073/pnas.2406783121](https://doi.org/10.1073/pnas.2406783121)
- Kempster, P., Li, D., Fielding, D. B., et al. 2025, *ApJL*, 990, L18, doi: [10.3847/2041-8213/adde55](https://doi.org/10.3847/2041-8213/adde55)
- Lambert, H. C., & Rickett, B. J. 1999, *ApJ*, 517, 299, doi: [10.1086/307181](https://doi.org/10.1086/307181)
- Mas-Ribas, L., McQuinn, M., & Prochaska, J. X. 2025, arXiv e-prints, arXiv:2504.19562, doi: [10.48550/arXiv.2504.19562](https://doi.org/10.48550/arXiv.2504.19562)
- McCourt, M., Oh, S. P., O’Leary, R., & Madigan, A.-M. 2018, *MNRAS*, 473, 5407, doi: [10.1093/mnras/stx2687](https://doi.org/10.1093/mnras/stx2687)
- McCourt, M., O’Leary, R. M., Madigan, A.-M., & Quataert, E. 2015, *MNRAS*, 449, 2, doi: [10.1093/mnras/stv355](https://doi.org/10.1093/mnras/stv355)
- Ocker, S. K., Chen, M. C., Oh, S. P., & Sharma, P. 2025, *APJ*, 988, 69, doi: [10.3847/1538-4357/ade0bc](https://doi.org/10.3847/1538-4357/ade0bc)
- Ocker, S. K., Cordes, J. M., & Chatterjee, S. 2021, *ApJ*, 911, 102, doi: [10.3847/1538-4357/abeb6e](https://doi.org/10.3847/1538-4357/abeb6e)
- Ocker, S. K., Cordes, J. M., Chatterjee, S., & Gorsuch, M. R. 2022, *ApJ*, 934, 71, doi: [10.3847/1538-4357/ac75ba](https://doi.org/10.3847/1538-4357/ac75ba)
- Pen, U.-L., & Levin, Y. 2014, *MNRAS*, 442, 3338, doi: [10.1093/mnras/stu1020](https://doi.org/10.1093/mnras/stu1020)
- Rickett, B. J. 1990, *ARAA*, 28, 561, doi: [10.1146/annurev.aa.28.090190.003021](https://doi.org/10.1146/annurev.aa.28.090190.003021)
- Rigby, J. R., Charlton, J. C., & Churchill, C. W. 2002, *APJ*, 565, 743, doi: [10.1086/324723](https://doi.org/10.1086/324723)
- Shin, K., Leung, C., Simha, S., et al. 2025, *APJ*, 993, 208, doi: [10.3847/1538-4357/ae093b](https://doi.org/10.3847/1538-4357/ae093b)
- Simard, D., & Pen, U.-L. 2018, *MNRAS*, 478, 983, doi: [10.1093/mnras/sty1140](https://doi.org/10.1093/mnras/sty1140)
- Squire, J., & Hopkins, P. F. 2017, *MNRAS*, 471, 3753, doi: [10.1093/mnras/stx1817](https://doi.org/10.1093/mnras/stx1817)
- Tumlinson, J., Peebles, M. S., & Werk, J. K. 2017, *ARA&A*, 55, 389, doi: [10.1146/annurev-astro-091916-055240](https://doi.org/10.1146/annurev-astro-091916-055240)
- Vedantham, H. K., & Ravi, V. 2019, *MNRAS*, 485, L78, doi: [10.1093/mnras/slz038](https://doi.org/10.1093/mnras/slz038)
- Wang, C., Oh, S. P., Jiang, Y.-F., & Kaul, I. 2025, *Monthly Notices of the Royal Astronomical Society*, staf1968, doi: [10.1093/mnras/staf1968](https://doi.org/10.1093/mnras/staf1968)
- Zhu, H., Baker, D., Pen, U.-L., Stinebring, D. R., & van Kerkwijk, M. H. 2023, *APJ*, 950, 109, doi: [10.3847/1538-4357/acdde0](https://doi.org/10.3847/1538-4357/acdde0)

APPENDIX

A. SCATTERING FROM A TURBULENT MEDIUM

For the sake of completeness, here we present a self-contained derivation of the volumetric scattering formulas developed elsewhere (Cordes & Rickett 1998; Cordes et al. 2016, 2022; Ocker et al. 2025). Consider a turbulent medium with electron density fluctuations given by

$$P_{\delta n_e}(q) = C_n^2 q^{-\beta} e^{-q^2/q_i^2}, \quad (q_o < q), \quad (\text{A1})$$

with outer and inner scales, $l_i = 2\pi/q_i$, $l_o = 2\pi/q_o$. Consider a slab of such a medium with thickness, L . We would like to compute the induced scattering time scale through the slab given the amplitude of the fluctuations and the inner and outer scale.

A.1. Mean ray deflection

First, we want to derive the mean square scattering angle that a ray undergoes when encountering a turbulent medium per unit distance through the medium. The bending angle that a ray traveling in the z -direction undergoes is given by transverse gradients in the phase along the ray:

$$\boldsymbol{\alpha} = \frac{\lambda}{2\pi} \nabla_{\perp} \phi. \quad (\text{A2})$$

The phase along a ray through a slab of thickness, s , is given by

$$\phi = \lambda r_e \int_0^s n_e(\mathbf{x}_{\perp}, z) dz, \quad (\text{A3})$$

where \mathbf{x}_{\perp} is the co-ordinate in the plane perpendicular to the line of sight. We are assuming that the bending angles are small so that we can approximate the phase of the true ray as the phase computed along a straight line in the z direction.

We want to compute the statistics of this quantity by relating it to the power spectrum of the density fluctuations. Using the Fourier convention

$$\delta n_e(\mathbf{x}) = \int d^3 \mathbf{q} \delta \tilde{n}_e(\mathbf{q}) e^{i\mathbf{q} \cdot \mathbf{x}}, \quad (\text{A4})$$

$$\langle \delta \tilde{n}_e(\mathbf{q}) \delta \tilde{n}_e^*(\mathbf{q}') \rangle = \delta^{(3)}(\mathbf{q} - \mathbf{q}') P_{\delta n_e}(q), \quad (\text{A5})$$

we can write the bending angle through a slab of thickness, s , as

$$\boldsymbol{\alpha} = \frac{\lambda^2 r_e}{2\pi} \int_0^s dz \int d^3 \mathbf{q} (i\mathbf{q}_{\perp}) \delta \tilde{n}_e(\mathbf{q}) e^{i(\mathbf{q}_{\perp} \cdot \mathbf{x}_{\perp} + q_z z)}. \quad (\text{A6})$$

It follows that the mean square bending angle is

$$\langle \alpha^2 \rangle = \frac{\lambda^4 r_e^2}{4\pi^2} \int_0^s dz \int_0^s dz' \int d^3 \mathbf{q} q_{\perp}^2 P_{\delta n_e}(q) e^{iq_z(z-z')}. \quad (\text{A7})$$

Differentiating this with respect to the slab thickness, s , and applying the Leibniz integral rule, we obtain

$$\frac{d\langle \alpha^2 \rangle}{ds} = \frac{\lambda^4 r_e^2}{4\pi^2} \int_{-s}^s dt \int d^3 \mathbf{q} q_{\perp}^2 P_{\delta n_e}(q) e^{iq_z t}. \quad (\text{A8})$$

Now, assuming the correlation lengths are small relative to the slab thickness, we let $s \rightarrow \infty$, so that the exponential in the integrand becomes a delta function, $2\pi\delta(q_z)$. Replacing $q_{\perp} = q \sin \theta$ and $q_z = q \cos \theta$, we arrive at

$$\begin{aligned} \frac{d\langle \alpha^2 \rangle}{ds} &= \frac{\lambda^4 r_e^2}{2\pi} \int q^2 dq d\Omega q^2 \sin^2 \theta P_{\delta n_e}(q) \delta(q \cos \theta), \\ &= \lambda^4 r_e^2 \int dq q^3 P_{\delta n_e}(q) \int d\theta \sin^3 \theta \delta(\cos \theta). \end{aligned} \quad (\text{A9})$$

The angular integral simply evaluates to unity. Following Cordes and Rickett, we call the mean deflection angle per unit length $\eta(s)$ and find

$$\eta(s) = \lambda^4 r_e^2 \int dq q^3 P_{\delta n_e}(q, s), \quad (\text{A10})$$

where in this last line we note that the power spectrum can also vary along the ray, so long as it does not vary faster than the outer scale of the turbulence.

Note that Cordes & Rickett (1998) define $\eta(s)$ from the second moment of the angular brightness distribution, computed from the visibility function $\langle E(\mathbf{x})E^*(\mathbf{x} + \mathbf{x}_\perp) \rangle = \exp(-0.5D_\phi(\mathbf{x}_\perp))$, where D_ϕ is the phase structure function (see e.g. Rickett 1990). In any case, one arrives at the same formula, Eq. A10.

A.2. Mean scattering time

With the mean ray deflection angle in hand, we can compute the mean scattering time that a point source will exhibit under ray optics. For a power spectrum of the form Eq. A1, one finds (Cordes & Rickett 1998):

$$\eta(s) = \frac{\lambda^4 r_e^2 \Gamma(3 - \beta/2)}{4 - \beta} q_i^{4-\beta} C_n^2(s), \quad (\text{A11})$$

assuming that the change in the power spectrum along the line of sight is limited to changes in the amplitude of the fluctuations and that $\beta < 4$.

We would like to relate the amplitude C_n^2 to the (slightly) more observable quantities such as the mean electron density and the variance of the electron density. Consider a single cloud. The variance of the perturbed electron density for a scale l is

$$\sigma_{n_e}^2 = \frac{2(2\pi)^{4-\beta} C_n^2 l^{\beta-3}}{\beta - 3} \quad (\text{A12})$$

for $\beta > 3$ and $l \gg l_i$. Thus, we can express the amplitude as

$$C_n^2 = K_\beta \epsilon^2 n_{e,c}^2 l_o^{3-\beta}, \quad (\text{A13})$$

where $n_{e,c}$ is the local average electron density of the cloud and we have defined $\epsilon = \sigma_{n_e,c}/n_{e,c}$ to be the fractional rms variance of the electron density perturbation at the outer scale of the cloud. We have also defined the constant $K_\beta \equiv (\beta - 3)/2(2\pi)^{4-\beta}$.

Now let us consider a medium filled with an ensemble of such cloudlets, taking up a fraction of the total volume, f_V . In this case, we must compute the volume-averaged amplitude:

$$\overline{C_n^2} = f_V K_\beta \langle \epsilon^2 n_{e,c}^2 \rangle l_o^{3-\beta}, \quad (\text{A14})$$

where here the line, $\overline{\cdot}$, denotes a volume average, and the angle bracket, $\langle \cdot \rangle$, denotes an ensemble average. It is common to define an additional parameter, $\zeta \equiv \langle n_{e,c}^2 \rangle / \langle n_{e,c} \rangle^2$, which characterizes the fractional variation in the internal electron density of individual clouds in the ensemble. Thus, we can write

$$\overline{C_n^2} = K_\beta \overline{n_e}^2 l_i^{4-\beta} \frac{\zeta \epsilon^2}{f_V l_o^{\beta-3} l_i^{4-\beta}} = K_\beta \overline{n_e}^2 l_i^{4-\beta} \tilde{F}, \quad (\text{A15})$$

where $\overline{n_e} = f_V \langle n_{e,c} \rangle$ is the average electron density over the entire volume. We have also assumed that every cloud has the same fractional rms fluctuations so that $\langle \epsilon^2 n_{e,c}^2 \rangle = \epsilon^2 \langle n_{e,c}^2 \rangle$. Finally, the fluctuation parameter is defined:

$$\tilde{F} \equiv \frac{\zeta \epsilon^2}{f_V l_o^{\beta-3} l_i^{4-\beta}}, \quad (\text{A16})$$

and the mean squared deflection angle per unit length through the medium is

$$\eta = A_\beta \lambda^4 r_e^2 \tilde{F} \overline{n_e}^{-2}, \quad (\text{A17})$$

where

$$A_\beta = \frac{1}{2} \frac{\beta - 3}{4 - \beta} \Gamma\left(3 - \frac{\beta}{2}\right). \quad (\text{A18})$$

The primary observable we are interested in is the scattering timescale. We can convert the mean square deflection per path length to the mean scattering time via:

$$\tau_{\text{mean}} = \frac{1}{2c} \int_0^{d_s} \eta(s) s \left(1 - \frac{s}{d_{so}}\right) ds. \quad (\text{A19})$$

For a thin screen of thickness, L , and a roughly constant $\eta(s)$ throughout, one arrives at

$$\tau_{\text{mean}} = \frac{d_{\text{eff}}}{2c} L \eta. \quad (\text{A20})$$

where $d_{\text{eff}} = d_{sl} d_{lo} / d_{so}$. In cosmological contexts, one must modify this to obtain

$$\tau_{\text{mean}} = \frac{d_{\text{eff}}}{2c} (1 + z_l)^{-3} L \eta, \quad (\text{A21})$$

where all the distance now refer to angular diameter distances, λ is the observing frequency, and z_l is the redshift of the scattering medium. One obtains a factor of $(1 + z_l)^{-4}$ as $\lambda \rightarrow (1 + z_l)\lambda$ in the bending angle formula (Eq. A17). An additional factor of $(1 + z_l)$ is obtained, since τ is defined as the phase delay of the rays at the observer, $\tau = d\phi_O / d\omega_O$, which differs from the phase at the scatterer by a factor of $(1 + z_l)$.

Together, Eqs. A17 and A21 provide the mean scattering time for an impulse scattered by a medium of thickness, L , filled with an ensemble of cloudlets making up a fraction of the total volume, f_V . We could, alternatively, consider a single cloudlet with $\tilde{F}_c = f_V \tilde{F}$. Then the scattering mean scattering angle through a single cloudlet of radius, r_c , is

$$\tau_{\text{mean},c} = \frac{d_{\text{eff}}}{2c} (1 + z_l)^{-3} r_c \eta_c, \quad (\text{A22})$$

$$\eta_c = A_\beta \lambda^4 r_c^2 \tilde{F}_l n_{e,c}^2. \quad (\text{A23})$$

Then, assuming that every cloudlet has the same fluctuation parameter, \tilde{F}_l and average density, $n_{e,c}$, the mean scattering time is simply given by

$$\tau_{\text{mean}} = \frac{d_{\text{eff}}}{2c} (1 + z_l)^{-3} L_{\text{tot}} \eta_c, \quad (\text{A24})$$

where L_{tot} is the total path length for which a given line of sight intersects the cloudlets. If the cloudlets are confined to a medium of thickness L and make up a fraction of the volume, f_V , then on average $L_{\text{tot}} = f_V L$. With $\tilde{F}_l = f_V \tilde{F}$ and $n_{e,c} = \bar{n}_e / f_V$, one sees that Eq. A24 is equivalent to Eq. A21.

The advantage of this formulation is that it gives us an easy way of computing the statistics of the observed scattering times. The primary focus of this paper is computing the TDF, i.e. $f_{\text{sc}}(> \tau)$. Thus, we are interested in the distribution of τ_{mean} for individual realizations of these cloudlet complexes. The key insight is that (assuming the cloudlets have uniform turbulent density fluctuation parameters), the variation in the observed scattering time is given precisely by the variation in the total path length intersecting the cloudlets, L_{tot} . The statistics of this intersection length is sensitive to the geometry of the cloudlets.

One subtlety to mention is that the actual observed scattering time is the $1/e$ timescale seen in FRB scattering tails. This is related to the mean scattering time by

$$\tau_{1/e} = A_\tau \tau_{\text{mean}}, \quad (\text{A25})$$

where A_τ is a constant that depends on the thickness of the scattering medium and the relation between the inner scale and the diffractive scale (Lambert & Rickett 1999). Since it does not change the shape of the scattering distributions, but shifts the mean by some constant offset, we will simply take $A_\tau = 1$.

A.3. The role of diffractive scattering (wave optics)

In the main text, we computed total scattering times using the mean deflection angle for rays through a turbulent medium under the assumption of ray (geometric) optics, neglecting diffractive contributions to the scattering time. Here we demonstrate that the diffractive contributions are negligible even when the inner scale of turbulent density fluctuations $l_i \ll r_{\text{diff}}$.

Diffractive optics produces angular deflections of order $\theta_{\text{diff}} = d_{\text{eff}} r_{\text{diff}}$, where r_{diff} is the transverse physical separation at which two rays will arrive at the observer with, on average, a radian offset in phase. For a medium with a power-law power spectrum, one finds (Ocker et al. 2025):

$$r_{\text{diff}} = \left[\beta \pi^2 2^{2-\beta} \frac{\Gamma(-\beta/2)}{\Gamma(\beta/2)} \lambda^2 r_e^2 L \overline{C_n^2} \right]^{1/(2-\beta)}. \quad (\text{A26})$$

Re-writing this in terms of the fluctuation parameters we have defined, one obtains

$$\begin{aligned} r_{\text{diff}} &= \left[N_\beta r_e^2 \lambda^2 L \overline{n_e^2} l_i^{4-\beta} \widetilde{F} \right]^{1/(2-\beta)}, \\ N_\beta &= \beta(\beta-3) 2^{\beta-3} \pi^{\beta-2} \frac{\Gamma(-\beta/2)}{\Gamma(\beta/2)}. \end{aligned} \quad (\text{A27})$$

Now the typical wavefront deflection angle produced by diffractive scattering is $\alpha_d = \lambda/2\pi r_{\text{diff}}$, which corresponds to a diffractive scattering time of

$$\tau_d = \frac{d_{\text{eff}}}{2c} \left(\frac{\lambda}{2\pi r_{\text{diff}}} \right)^2 \quad (\text{A28})$$

We would like to compare this diffractive scattering time to the refractive (ray) scattering time of the previous section to determine which one predominates. To do so, we can re-write the diffractive scale in terms of the mean square deflection angle of the previous section, finding:

$$r_{\text{diff}} = \left[\frac{N_\beta}{A_\beta} \lambda^{-2} l_i^{4-\beta} L \eta \right]^{1/(2-\beta)}. \quad (\text{A29})$$

Then

$$\tau_d = \frac{d_{\text{eff}}}{8\pi^2 c} \left(\frac{N_\beta}{A_\beta} \right)^{2/(\beta-2)} (l_i/\lambda)^{2(4-\beta)/(\beta-2)} (L\eta)^{2/(\beta-2)}. \quad (\text{A30})$$

Now, consider the quantity r_{diff}/l_i . This can be written as

$$\frac{r_{\text{diff}}}{l_i} = \left(\frac{N_\beta}{A_\beta} \right)^{-1/(\beta-2)} (l_i/\lambda)^{-2/(\beta-2)} (L\eta)^{-1/(\beta-2)}. \quad (\text{A31})$$

Thus, whenever $r_{\text{diff}} \gg l_i$, we also have that

$$(\lambda/l_i)^2 \gg \frac{N_\beta}{A_\beta} L\eta, \quad (\text{A32})$$

from which it follows:

$$\begin{aligned} \tau_d &\ll \frac{d_{\text{eff}}}{8\pi^2 c} \left(\frac{N_\beta}{A_\beta} \right)^{2/(\beta-2)} \left(\frac{N_\beta}{A_\beta} \right)^{-(4-\beta)/(\beta-2)} (L\eta)^{-(4-\beta)/(\beta-2)} (L\eta)^{2/(\beta-2)}, \\ &\ll \frac{d_{\text{eff}}}{8\pi^2 c} \frac{N_\beta}{A_\beta} L\eta, \\ &\ll \frac{N_\beta}{4\pi^2 A_\beta} \tau_{\text{mean}}, \end{aligned} \quad (\text{A33})$$

assuming $2 < \beta < 4$. For Kolmogorov turbulence ($\beta = 11/3$), the constant $N_\beta/4\pi^2 A_\beta \approx 2.8$. Thus, when the inner scale is much less than the diffractive scale (or, equivalently, when $\lambda/l_i \gg \sqrt{L\eta}$), the refractive mean scattering time exceeds the diffractive scattering time. For simplicity, we will assume this is the case, and only apply the ray optics formulae for the scattering time. However, we note that, whereas the mean refractive scattering time scales exactly linearly with the effective intersection length, for a Kolmogorov turbulent medium, the diffractive scattering time scales nearly linearly: $\tau_d \propto L^{6/5}$. Thus, we argue that qualitatively, our results will be similar for the $r_{\text{diff}} \ll l_i$ regime. The regime where diffractive optics transitions to refractive optics, $l_i \sim r_{\text{diff}}$, is not well characterized and may require more advanced wave optics techniques .

B. REFRACTIVE SLAB

In this section, we compute the characteristic bending angle for a slab with electron density n_e , thickness δ , and length Λ , as a function of its inclination angle ι with respect to the line of sight. Since the bending angle a ray undergoes when encountering free electrons is simply determined by the transverse gradient in the excess electron column, we need to estimate the excess column density of the slab. As can be seen from Fig. 8, the column density of a thin slab is given by $N_e = n_e l_{\parallel} = n_e \delta / \cos \iota$. Thus, a face-on sheet ($\iota = 0$) has a column density of $n_e \delta$. If the slab were infinitely long, an edge-on slab ($\iota = \pi/2$) would have an infinite column density as $\cos \iota \rightarrow 0$. However, for a physical slab with finite length Λ , we will take the column density to be simply

$$N_e(\iota) = \min \left\{ \frac{n_e \delta}{\cos \iota}, n_e \Lambda \right\}. \quad (\text{B34})$$

To estimate the transverse gradient of the column density, we need to know the transverse scale over which the column density varies. This is set by $l_{\perp} = \min \{ \delta / \sin \iota, \Lambda \}$. We can thereby estimate the transverse column density gradient as $\nabla_{\perp} N_e \sim n_e l_{\parallel} / l_{\perp}$. From this, we obtain the maximum bending angle that such a slab can produce is

$$\alpha_{\max}(\iota) = \frac{\lambda^2 r_e}{2\pi} \nabla_{\perp} N_e \sim \frac{\lambda^2 r_e n_e}{2\pi} \min \{ \tan \iota, A \}, \quad (\text{B35})$$

where $A = \Lambda / \delta$ is the aspect ratio of the sheet. The bending angle increases with inclination until it saturates to some maximum value determined by A . There is also a minimum value that is reached as $\iota \rightarrow 0$, due to the largest possible value of $l_{\perp} = \Lambda$; however, since in this work we are concerned with the cumulative distribution function of scattering timescales above some value, we will simply neglect this minimum value. Now, for a corrugated sheet, which we model as an organized ensemble of such slabs, we will take the characteristic bending angle to be half this maximum angle, defining:

$$\alpha_{\text{sheet}}(\iota) = \frac{\lambda^2 r_e n_e}{4\pi} \min \{ \tan \iota, A \}. \quad (\text{B36})$$

Now, in order to predict the scattering timescale statistics for a complex of such slabs, we would like to know the the average number of slabs intersected by a given line of sight. For a complex of size R and a volume filling factor, f_V , of slabs, the average path length intersecting such slabs is $f_V R$. To compute the average number of slabs contributing to this path length, we need to know the average path length through a single slab integrated over arbitrary inclination angles. For a slab with large aspect ratio ($A \gg 1$), we can split this integral into two parts. When the slab is inclined by $\iota > \frac{\pi}{2} - A^{-1}$, we will consider this to be edge on, so that the path length along the line of sight through the slab is simply given by the total length, Λ . When the slab is inclined by $\iota < \frac{\pi}{2} - A^{-1}$, the intersection length is given by $\delta / \cos \iota$. We want to average this over the solid angle $d\Omega = \sin \iota d\iota d\phi$. Thus, we obtain the average intersection length through a single slab to be:

$$\begin{aligned} \bar{l}_{\parallel} &= \int_{\iota=0}^{\iota=\pi/2-A^{-1}} \frac{\delta}{\cos \iota} d\Omega + \int_{\iota=\pi/2-A^{-1}}^{\iota=\pi/2} \Lambda d\Omega, \\ &= -2\pi\delta \log(\sin A^{-1}) + 2\pi\Lambda \sin A^{-1}, \\ &\approx 2\pi\delta(1 + \log A), \end{aligned} \quad (\text{B37})$$

where the last line is obtained for $A \gg 1$. It follows that the average number of slabs intersected by a given line of sight is $N_c = f_V R / \bar{l}_{\parallel}$:

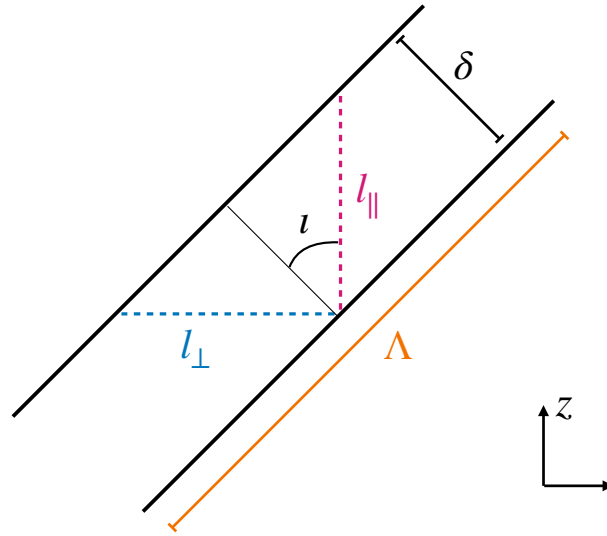


Figure 8. Diagram of an inclined slab of scattering material with length Λ and width δ . The vertical z -axis is the line of sight and ι is the inclination angle. The lengths l_{\parallel} and l_{\perp} define length-scales of the slab projected parallel and perpendicular to the line of sight, respectively.